Journal of Alloys and Compounds 1047 (2025) 185066

Contents lists available at ScienceDirect

Journal of Alloys and Compounds

journal homepage: www.elsevier.com/locate/jalcom

In-situ HEXRD study on the β→α transformation in Al alloy EN AW-6063

Nicolás García Arango [a,b,*], Roman Schuster [b,c], Robert Kahlenberg [b,d], Philipp Timm [b], Lukas Helml [b], Philipp Retzl [b], Andreas Stark [e], Erwin Povoden-Karadeniz [a,b]

[a] Christian Doppler Laboratory for Interfaces and Precipitation Engineering CDL-IPE, TU Wien, Getreidemarkt 9, Vienna 1060, Austria
[b] Institute of Materials Science and Technology, TU Wien, Getreidemarkt 9, Vienna 1060, Austria
[c] Department of Lithospheric Research, University of Vienna, Josef-Holaubek-Platz 2, Vienna 1090, Austria
[d] Materials Center Leoben Forschung GmbH, Vordernberger Straße 12, Leoben 8700, Austria
[e] Institute of Materials Research, Helmholtz-Zentrum Geesthacht, Geesthacht, Germany

ARTICLE INFO

Keywords:
Phase transformation
In-situ high-energy X-ray diffraction
Aluminium alloys
Homogenization treatment
Nucleation & Dissolution

ABSTRACT

The present study employs in-situ high-energy X-ray diffraction (HEXRD) to investigate the β-AlFeSi→α-Al(Fe, Mn)Si transformation in a 6063 Al alloy during homogenization heat treatment. The characteristics of HEXRD, combined with the experimental setup, enable an evaluation of the evolution of individual diffraction peaks as a function of temperature and time. The diffraction intensity evolution is then used to quantify the transformation into phase fractions using the reference intensity ratio (RIR) method. The β-AlFeSi→α-Al(Fe,Mn)Si transformation is measured at the homogenization temperatures: 540, 550, 560, 570, 580, 590, and 600 °C. In addition, three heating rates (4, 50, 100 °C/min) are studied to observe the influence of the heating stage on the transformation onset. The growth of α at the expense of β dissolution is faster at higher temperatures, and is limited by the diffusion of Mn. At the same time, during the heating ramp, the evolution of α and β fractions indicates a two-stage transformation, characterized by different growth rates of α.

1. Introduction

The microstructure of as-cast industrial 6xxx series Al alloys typically contains micrometer-sized intermetallic phases located along the Al grain boundaries [1,2]. Their formation is in particular attributed to the limited solid solubility of Fe in the Al matrix [3,4]. The structure of the intermetallic phases depends on the composition and solidification conditions, such as the cooling rate, thermal gradients, and added grain refiners [5–9]. For commercial 6xxx series Al alloys containing Fe and Mn, monoclinic β-AlFeSi and cubic α-Al(Fe,Mn)Si are the two most prominent intermetallic phases [10–12]. β-AlFeSi negatively impacts the extrudability and surface quality of the material due to its sharp-faced morphology and high hardness, which promote crack initiation and propagation at the β/Al matrix interface [13,14]. In contrast, α-Al(Fe,Mn)Si, with its more rounded morphology, is preferred over β-AlFeSi, as it improves the hot formability and ductility of the material [15,16].

The addition of Mn in Al 6xxx alloys shifts the intermetallic stability region from β-AlFeSi towards α-Al(Fe,Mn)Si [17,18]. The incorporation of Mn promotes the formation of α at the expense of β during solidification and subsequent homogenization. This phase transition is often referred to as β→α transformation [19]. In Al alloys of the 6xxx series, the objectives of homogenization are the transformation of intermetallic phases, the reduction of micro- and macrosegregations, the nucleation of dispersoids [20], and the dissolution of other primary particles such as Mg_2Si and Si [21]. Homogenization is typically conducted within a temperature range of 480 and 590 °C, and may extend to 12 h [21–23].

Various techniques have been described to quantify the β→α transformation [24]. One common approach involves ex-situ optical image analysis at specific homogenization time-temperature conditions, where β and α phases are identified purely based on their distinct morphologies [25]. Additionally, a combination of SEM imaging with energy-dispersive X-ray spectroscopy (EDX) has been employed to classify intermetallic phases as either β or α based on the measured (Fe+Mn)/Si ratios [26]. Another method involves the selective dissolution of the matrix, followed by conventional X-ray analysis of the residual material [22,27].

A prior in-situ transmission electron microscopy (TEM) study investigated the onset of the β→α transformation during the thermal

* Corresponding author at: Christian Doppler Laboratory for Interfaces and Precipitation Engineering CDL-IPE, TU Wien, Getreidemarkt 9, Vienna 1060, Austria.
E-mail address: nicolas.arango@tuwien.ac.at (N.G. Arango).

https://doi.org/10.1016/j.jallcom.2025.185066
Received 25 September 2025; Received in revised form 3 November 2025; Accepted 16 November 2025
Available online 17 November 2025
0925-8388/© 2025 The Author(s). Published by Elsevier B.V. This is an open access article under the CC BY license (http://creativecommons.org/licenses/by/4.0/).

ramp-up to the homogenization temperature [28]. α nucleation was observed to initiate at approximately 450 °C, with new α particles forming preferentially along the β needles. These α particles later grew at the expense of the parent β particles as the temperature increased. The transformation kinetics, studied in [29], showed a significant effect of Mn on the transformation rate, while the influence of both Fe and Si is regarded as more modest.

The present work is the first to utilize synchrotron-based high-energy X-ray diffraction (HEXRD) to study the β→α phase transformation. Due to the intensity, high brilliance, and monochromatic, collimated beams, synchrotron radiation is widely used to study and characterize a wide range of materials, such as bio- and nanomaterials, energy-storing and metallic materials, among others [30–32]. In particular, for Al-based materials, HEXRD has been employed to investigate the evolution of hardening and non-hardening phases in 6xxx and 7xxx series Al alloys [33–36], and the microstructural changes occurring during the homogenization of 3xxx series Al alloys [37].

In the present study, the β→α transformation is tracked as a function of the homogenization conditions by evaluating the change in the diffractograms during the selected heat treatments. The characteristic high brilliance of the incoming beam and the detection features of the experiment, such as the recording of a diffractogram every four seconds, enabled a highly accurate, time-resolved study. The effect of the heating stage on the early stages of the transformation is investigated with varying heating rates, while the transformation kinetics is studied at seven homogenization temperatures: 540, 550, 560, 570, 580, 590, and 600 °C.

2. Materials and methods

2.1. Material

The composition of the EN AW-6063 alloy is shown in Table 1. The Al ingots were produced by Neuman Aluminum via direct chill casting. The material is used in its as-cast condition. Samples were extracted from the central region of the billet and machined into cylindrical shapes with a radius of 5 mm and a length of 10 mm. The average grain size is approximately 100 μm.

Scheil-Gulliver and equilibrium calculations are performed using the software MatCalc [38] and its latest thermodynamic Al database [39], with the results presented in Figs. 1a and 1b, respectively. Consistent with experimental observations discussed in 2.3, the Scheil-Gulliver calculation identifies β-AlFeSi as the predominant intermetallic phase in the as-cast microstructure. Additionally, primary Mg_2Si, silicon, and α-Al(Fe,Mn)Si particles are present, albeit in significantly lower fractions compared to β-AlFeSi. The solidification begins at 654 °C, as Al-fcc grains start to form. The Scheil-Gulliver calculation is performed until the remaining liquid fraction in the microstructure is approximately 0.05 %.

In contrast to the Scheil-Gulliver solidification calculation (Fig. 1a), equilibrium conditions (Fig. 1b) indicate that the α-Al(Fe,Mn)Si phase is the thermodynamically stable intermetallic compound in the system. Within the considered temperature range, β-AlFeSi phase is therefore metastable and thus expected to dissolve in favor of α as the system evolves toward equilibrium, provided that the necessary kinetic conditions are met. The presence and evolution of Mg_2Si and silicon particles will not be studied further as they do not interfere with the β→α transformation.

Table 1
Chemical composition of the Al 6063 samples in mass percent.

Si	Fe	Mg	Mn	Cu+Cr+Zn+Ti	Al
0.6	0.23	0.47	0.05	0.05	Bal.

2.2. In situ diffraction experiments

The in situ HEXRD experiments were performed at the P07 High Energy Materials Science beamline of the high brilliance 3rd Generation storage ring PETRA III at the Deutsches Elektronen Synchrotron (DESY) in Hamburg, Germany [40].

To study the β→α transformation, two experimental blocks are conducted. For the first series of experiments, three different heating rates (4, 50, and 100 °C/min) are applied from room temperature (20 °C) up to the homogenization temperature of 560 °C. This is followed by an isothermal holding time at 560 °C of 2 h for both the 50 and 100 °C/min rates. For the 4 °C/min heating rate, a shorter holding time of 10 min is applied due to technical issues. In the second series of experiments, the homogenization temperature is varied while maintaining a constant heating rate of 50 °C/min. Experiments are conducted at 540, 550, 560, 570, 580, 590, and 600 °C, with holding times of up to 2 h for the lower temperatures. All samples are subsequently cooled under helium at a rate of 50 °C/min. The applied temperature profiles for both experimental blocks are illustrated in Fig. 2.

To ensure precise temperature control, each sample is initially spot-welded to a Type-K thermocouple and then placed inside the induction heating coil of the Bähr 805 A/D dilatometer, installed at the P07 experimental hutch. In the dilatometer, the sample is held longitudinally by two quartz rods. The induction coil features an aperture designed to enable the beam to traverse the sample without causing interference. The thermocouples are carefully placed to prevent their interaction with the beam. The sample is maintained under vacuum during the heat treatment to inhibit the formation of an oxide layer on its surface.

The HEXRD experiments are conducted using a monochromatic beam with a photon energy of 87.098 keV, equivalent to a wavelength $\lambda = 0.14235$ Å. The beam is limited by two slits to a rectangular section of 700×700 μm^2. As the beam traverses the radial axis of the sample, transmission X-ray diffractograms, in the form of Debye-Scherrer rings, are recorded with a flat panel 2D Perkin Elmer XRD 1621 detector located at approximately 1100 mm from the sample. An illustration of the experimental setup is shown in Fig. 3. Using a time resolution of four seconds per recorded diffractogram, each experiment generates data in the order of a thousand data files, allowing for a detailed in-situ investigation of the microstructural evolution.

Each Debye-Scherrer ring recorded is associated with the diffraction of a specific crystallographic plane of one phase present in the microstructure. However, different phases can produce diffraction rings at the same location, so that possible overlaps must be considered. Measuring the variation in diffraction intensity during the heat treatment provides insight into the evolution of the multiple phases that comprise the microstructure. For the studied Al-based alloy, the largest diffraction contributions originate from the Al matrix, and its peaks will overshadow those of other phases located in their vicinity. To evaluate the β→α transformation, it is necessary to analyze the diffraction rings originating from β and α phases that are spatially separated from the characteristic Al matrix diffractions.

The azimuthal integration of the 2D Debye-Scherrer rings into 1D diffraction patterns is done using the FIT2D software [41]. To calibrate the experimental conditions, such as the distance between the sample and the detector and the tilt angle formed by the incident beam and the detector, the diffraction of a standard 5 mm width LaB6 powder sample was measured under the same experimental conditions at room temperature.

2.3. Phase identification and data evaluation

The phase identification and peak indexing are done using the HighScore Plus XRD analysis software from Malvern Panalytical [42]. With an incoming beam of wavelength $\lambda = 0.14235$ Å, the region of interest extends over a range of $1.5° < 2\theta < 6.5°$.

The crystal information of α and β is included in Table 2. α-Al(Fe,Mn)

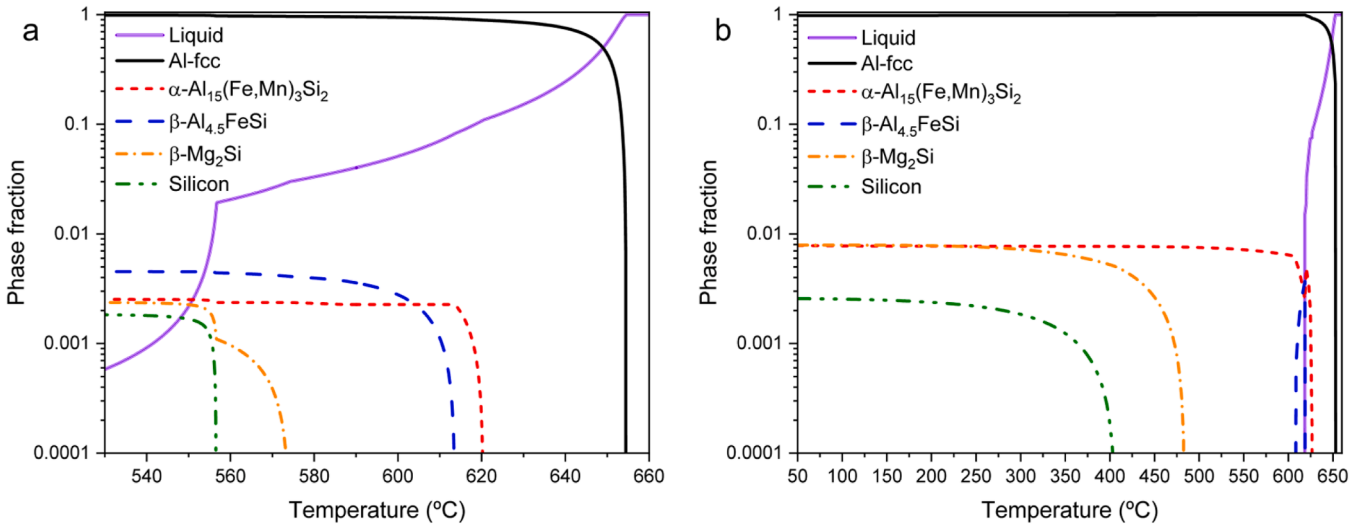

Fig. 1. Solidification of the 6063 Al alloy, a) Scheil-Gulliver calculation, with β-AlFeSi being the principal intermetallic phase in the as-cast state, and b) equilibrium calculation, showing α-Al(Fe,Mn)Si as the equilibrium intermetallic phase in most of the temperature range.

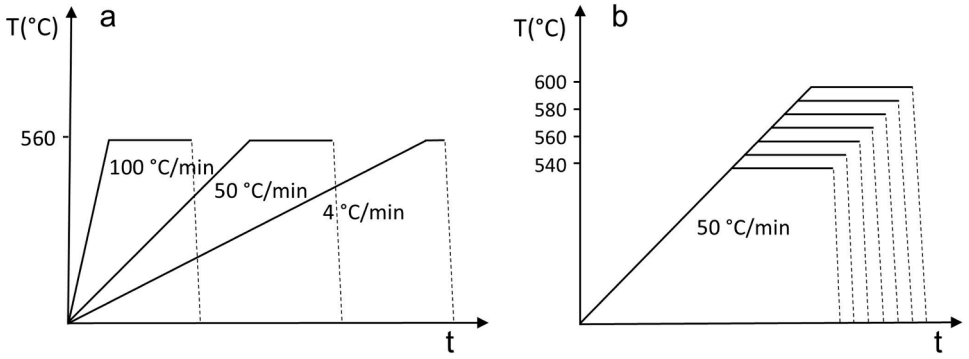

Fig. 2. Overview of in-situ heat treatments in the present study. (a) Heating to the homogenization temperature (560 °C) at three different rates: 4, 50, and 100 °C/min. (b) Heating at 50 °C/min to the homogenization temperatures: 540, 550, 560, 570, 580, 590, and 600 °C, followed by an isothermal step for 2 h.

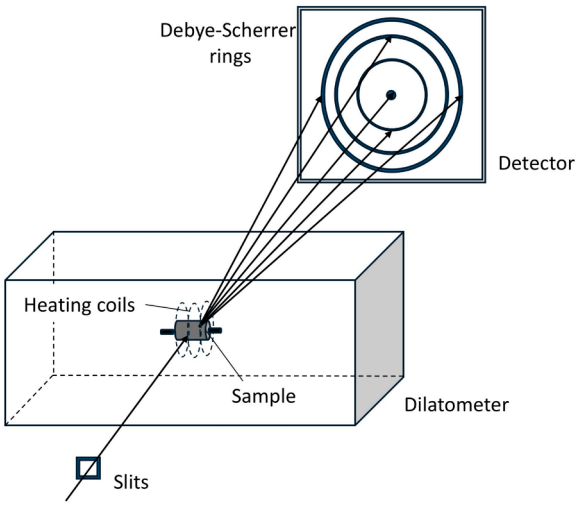

Fig. 3. Experimental setup for the in situ experiments.

Si is an extension of cubic α-AlMnSi with Fe substituting Mn atoms [3]. As a result, several compositions for α have been reported [3,43,44]. Its lattice parameter varies between 12.5 and 12.65 Å as a function of the Fe/Mn ratio [3,27]. Contrary to α, β-AlFeSi is a stochiometric phase,

Table 2
Composition, crystal structure, and unit cell parameters of α-Al(Fe,Mn)Si and β-AlFeSi.

Phase	Crystal structure	Unit cell	Reference
α-$Al_{15}(Fe,Mn)_3Si_2$, α-$Al_{16}Mn_4Si_3$, α-$Al_{19}Fe_4MnSi_2$	Pm-3	a= 12.5 Å (31.1 % Fe) a= 12.65 Å (0 % Fe)	[3,43,44]
β-$Al_{4.5}FeSi$	A2/a	a= 6.161 Å, b= 6.175 Å, c= 20.81 Å, β= 90.42	[45,46]

with the substitution between Fe and Mn atoms being insignificant [45,46]. A schematic representation of the atomic structure of α-$Al_{15}(Fe,Mn)_3Si_2$ and β-$Al_{4.5}FeSi$ is shown in Fig. 4.

During homogenization, as the β→α transformation unfolds, the diffraction of the sample changes. These changes are shown in Fig. 5, where β-related diffraction peaks (identified in blue), which are dominant at the beginning of the heat treatment, weaken as temperature increases. At the same time, the peaks related to α (marked in red) appear. The y-axis in Fig. 5 is plotted on a logarithmic scale to magnify the peaks from α and β, which would be overshadowed by the much larger Al-fcc matrix peaks.

Table 3 provides a summary of the crystallographic data for the

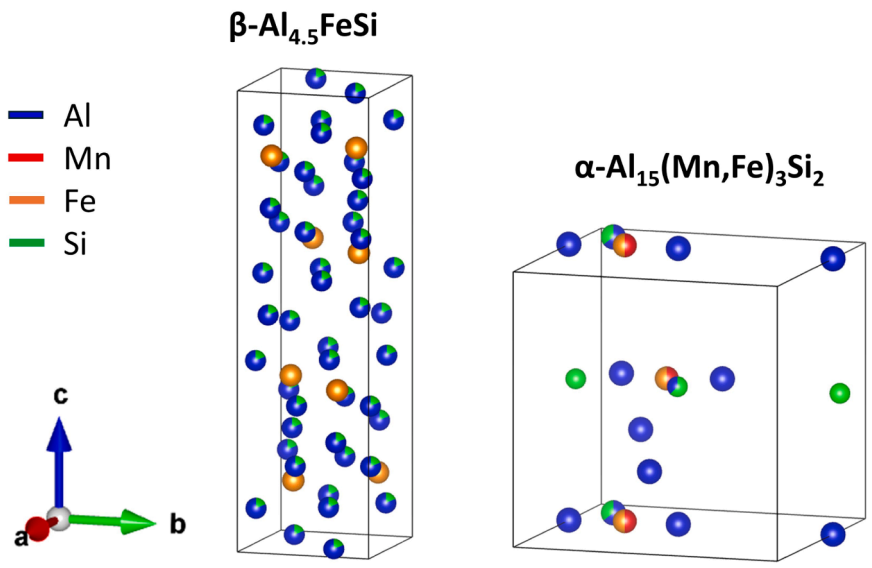

Fig. 4. Schematic representation of the atomic structure of α-$Al_{15}(Fe,Mn)_3Si_2$ and β-$Al_{4.5}FeSi$.

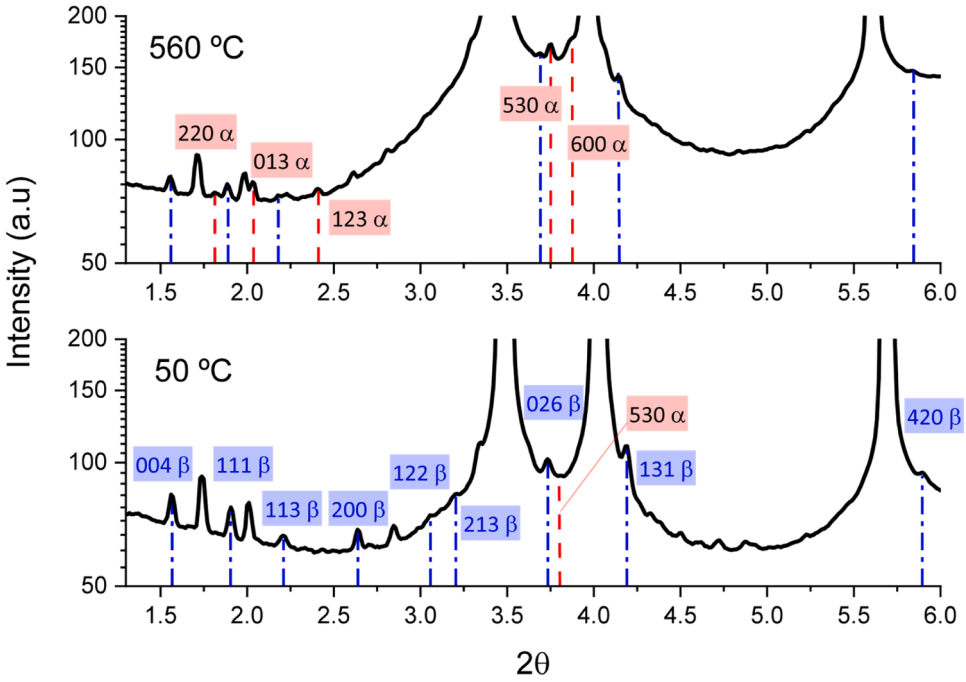

Fig. 5. Integrated 1D diffractograms at 50 °C (down) and 560 °C (up), β-$Al_{4.5}FeSi$-related peaks are identified in blue, and α-$Al_{15}(Fe,Mn)_3Si_2$-related peaks are marked in red. The associated diffracting plane of each peak is included in the labels.

studied intermetallic phases present in the microstructure. For each phase, it contains the theoretical 2θ position of each diffraction line at room temperature, its related plane (hkl), and relative intensity, measured against its strongest diffracting plane. For clarity, only those peaks with the higher relative intensity are included. For the evaluation, it is not possible to study peaks from α and β overlapping with those from the Al matrix. Using the HighScore Plus software together with the ICDD database [47], the reference codes for the indexing of α-$Al_{15}(Fe,Mn)_3Si_2$ and β-$Al_{4.5}FeSi$ are ICDD: 01–087–0528 and ICDD: 04–007–1803, respectively, obtained from sources [43] and [45].

The evolution of α and β is investigated based on the changes in the diffraction patterns. A Python-based program has been developed to identify and measure the area intensity of specific peaks in the diffractograms. The diffraction intensity is defined by the peak area rather than its maximum, as the area represents the total sum of detected diffracted X-ray photons. In contrast, the maximum is more influenced by the experimental conditions of the device, as well as micro strains, particles, and grain sizes. The intensity is computed throughout the entire heat treatment using a loop that processes the complete dataset. It calculates the diffraction intensity of a peak individually, associating time and temperature-related information with each diffractogram using a file generated by the dilatometer software. A more detailed description of the developed software is provided in Reference [36].

Temperature-related effects influence the diffraction and should therefore be considered in the analysis. Temperature variations affect the interplanar distances d, shifting the peak position, according to Bragg's law. As the temperature increases, so does the amplitude of thermal vibrations, here denoted as δu [48]. As thermal vibrations

Table 3
α and β-related peaks used for the phase identification: diffracting plane (hkl), 2θ position, and peak relative intensity at room temperature.

α-$Al_{15}(Fe,Mn)_3Si_2$			β-$Al_{4.5}FeSi$		
220	1.82	8.7	004	1.56	100
013	2.04	30.2	111	1.91	68.5
123	2.4	10	113	2.2	10.4
510	3.29	11.9	020	2.64	32.5
521	3.53	12.4	122	3.05	38.5
530	3.76	62.9	213	3.19	33.7
600	3.87	27.8	026	3.53	22.5
235	3.97	100	220	3.74	72.1
149	6.38	27.1	019	3.77	35.3
			126	3.78	26.7
			031	3.98	70.1
			217	4.04	28.6
			028	4.1	39.3
			131	4.19	87.6

increase, the periodicity of the lattice is reduced proportionally to δu/d, thus weakening the diffraction intensity [48]. For a given thermal vibration δu, this effect is particularly relevant for smaller interplanar distances, i.e. peaks located at higher 2θ angles, where δu/d is larger. In addition, temperature-diffuse scattering results in increased background scattering throughout the entire diffractogram, although this effect is more significant for higher 2θ angles [49].

During the heat treatments, changes in the diffractograms are governed by both microstructural evolution and temperature-related effects, the latter of which may hinder the analysis of β and α. To account for the influence of temperature, it can be assumed that the Al fraction in the system remains constant. Hence, all changes in its diffraction signals measured during the heat treatment are attributed to temperature-related phenomena. Temperature-related effects are therefore minimized in the analysis via the RIR method by normalizing the intensity evolution of the β and α-related peaks with that of the nearest Al peak.

2.4. RIR method for quantitative analysis

There is a direct correlation between diffracted intensity and phase fraction, which can be used to quantify the amount of a given constituent in a mixture. This relation is not linear, as it depends on the absorption coefficient of the constituent, which is itself a function of its own concentration in the system. Most quantitative analyses compare the diffraction intensity of a phase to a standard reference. The standard reference line can be related to another crystalline constituent in the system (direct comparison method), to a diffraction peak from a pure sample of the analyzed phase (external standard method), or to the diffraction from an external material mixed within the material (internal standard method) [48].

The Reference Intensity Ratio (RIR) method belongs to the internal standard methods, for which a constant $RIR_{\alpha,s}$ value (s denotes a different phase from α) is defined as:

$$RIR_{\alpha,s} = \frac{I_{i\alpha}}{I_{js}} \frac{I_{js}^{rel}}{I_{i\alpha}^{rel}} \frac{X_s}{X_\alpha} \quad (1)$$

Where $I_{i\alpha}$ is the calculated intensity of diffraction line i corresponding to phase α, I_{js} is the calculated intensity of diffraction line j corresponding to phase s, $I_{i\alpha}^{rel}$ and I_{js}^{rel} are the relative intensities of diffraction lines i and j with respect to their peak of maximum intensity; X_α and X_s are the weight fractions of phases α and s, respectively [50].

Corundum is commonly used as the universal reference material to which the highest diffracting lines from phase α and corundum ($I/I_{Corundum}$) in a 50 % weight mixture are measured. Having standard RIR values allows the reference intensity ratio of phase α related to phase s to be obtained as:

$$RIR_{\alpha,s} = \frac{RIR_{\alpha,c}}{RIR_{s,c}} \quad (2)$$

c being corundum or any other chosen phase of reference.

Rearranging Eqs. 1 and 2, the relative fraction of phase α with respect to another phase β within the system can be calculated as:

$$\frac{X_\alpha}{X_\beta} = \frac{I_{i\alpha}}{I_{j\beta}} \frac{I_{j\beta}^{rel}}{I_{i\alpha}^{rel}} \frac{RIR_{\beta,c}}{RIR_{\alpha,c}} \quad (3)$$

Eq. 3 enables the analysis of mixtures with crystalline phases when the RIR values are known. For this calculation, four experimental constants are required ($I_{i\alpha}^{rel}$, $I_{j\beta}^{rel}$, $RIR_{\alpha,c}$, $RIR_{\beta,c}$).

Applied to the β→α transformation and to limit the calculation from 0 (where no α is formed) to 1 (where only α is present), the RIR equation for the α fraction will be computed as $X_\alpha/(X_\beta+X_\alpha)$:

$$\frac{X_\alpha}{X_\beta + X_\alpha} = \frac{1}{\frac{X_\beta}{X_\alpha} + 1} = \frac{1}{\frac{I_{j\beta}}{I_{i\alpha}} \frac{I_{i\alpha}^{rel}}{I_{j\beta}^{rel}} \frac{RIR_{\alpha,c}}{RIR_{\beta,c}} + 1} \quad (4)$$

The diffracting planes and the RIR constants used for the calculation are included in Table 4. RIR values are obtained from the same database detailed in 2.3.

3. Results and discussion

3.1. Effect of the heating rate on the β→α transformation

The onset of the β→α transformation occurs during the heating to the homogenization temperature [28,51]. The start of α nucleation and β dissolution is studied for the three selected heating rates (4, 50, and 100 °C/min).

The evolution of α is shown in Fig. 6. It is evaluated by the change in intensity of the second most prominent diffraction peak, corresponding to the (530) plane, located at $2\theta = 3.76°$ (see Table 3). The highest diffracting α peak, associated with the (235) plane, overlaps with an Al-fcc diffraction centered at $2\theta = 3.97°$, rendering it ineffective for its evaluation. Despite β being the predominant intermetallic phase in the as-cast state, a relatively weak diffraction signal from the strongest α peaks confirms the Scheil-Gulliver prediction (Fig. 1) of a proportionally small initial α fraction present in the microstructure.

The increase of α intensity begins at 430 °C for the slower heating rate (4 °C/min), and around 460–480 °C for the higher rates (50 and 100 °C/min)—a comparable temperature range to be reported for α nucleation by Reference [28]. For the 4 °C/min heating, a sharp increase in the α signal is recorded starting at 550 °C. This increase in α intensity is not observed during heating at the faster rates of 50 and 100 °C/min. Upon reaching the homogenization temperature, 560 °C, the α fraction is highest for the slowest heating rate. Both effects can be attributed to the larger time spent at higher temperatures during slow heating, which allows for more element diffusion, needed for the transformation. During holding at 560 °C, the amount of α increases steadily over time. At a given time during the holding stage, the α fraction is always lower when higher heating rates are applied. The heating speed does not appear to affect the transformation mechanism, as the shape of α evolution curves at the isothermal stage remains unchanged.

To evaluate the evolution of β, its strongest-diffracting peak, corresponding to the (004) plane, located at $2\theta = 1.56°$, is used. The effect of

Table 4
Indices of the diffracting planes and RIR values used for the α and β quantification.

α-$Al_{15}(Fe,Mn)_3Si_2$				β-$Al_{4.5}FeSi$			
hkl	2θ	Intensity [%]	$RIR_{\alpha,c}$	hkl	2θ	Intensity [%]	$RIR_{\beta,c}$
530	3.76	62.9	2.4	004	1.56	100	0.79

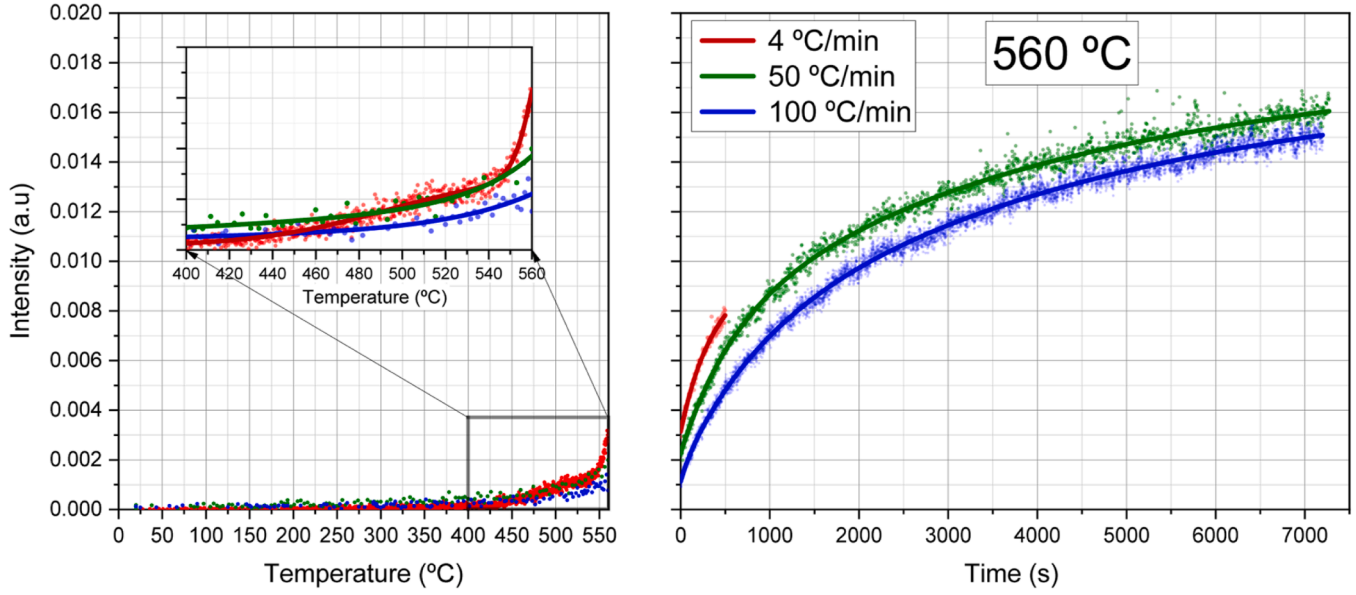

Fig. 6. Evolution of α as a function of temperature from room temperature to 560 °C at three heating rates (4, 50, and 100 °C/min), including an isothermal holding stage at 560 °C. Each data point corresponds to a calculated diffraction intensity, while the solid line represents the average trend of the evolution.

the heating rate on the evolution of β is shown in Fig. 7. During the heating stage, β dissolution, indicated by a reduction in its diffraction intensity, is only noticeable around 535–540 °C at the slowest heating rate of 4 °C/min. Upon reaching 560 °C, a decrease in intensity of nearly 25 % is measured. Contrary to α (Fig. 6), no change in the intensity is observed for the faster rates during the heating ramp. The unfold of β dissolution during the holding stage (Fig. 7, right side) is considerably different for the slowest heating rate applied, where a larger intensity reduction is observed. No substantial differences in β evolution are measured in the samples heated at 50 and 100 °C/min.

The rapid signal increase of α at 550 °C for the slowest heating rate (4 °C/min) seen in Fig. 6 is preceded by the start of β dissolution at 540 °C. This suggests a two-stage phase transformation: An initial stage, observed at all heating rates, beginning between 430 and 480 °C, where α nucleates and grows independently from β dissolution, and a second part, seen only for the slowest rate (4 °C/min), for which a decrease in β fraction (starting at 540 °C), results in an increase of the rate at which α grows (at 550 °C), probably due to a local excess in element availability near the α particles. This second stage in α evolution is delayed to the holding stage at 560 °C for the faster heating rates of 50 and 100 °C/min, as β starts to dissolve.

3.2. *Quantification of the β→α transformation during the heating ramp*

The measured intensity evolution of α and β-related peaks during the heat treatments is used to quantify their transformation using the RIR method, as explained in 2.4. The variable used for quantification is the relative fraction of α with respect to the sum of α and β relative fractions: $X_\alpha/(X_\alpha+X_\beta)$. The extent of the transformation during the heating stage, at a rate of 4 °C/min up to 560 °C, is shown in Fig. 8a. The relative fraction of α increases steadily from an initial value of 0.31 to 0.55 as the temperature reaches 550 °C, after which a rapid α increase of 20 %

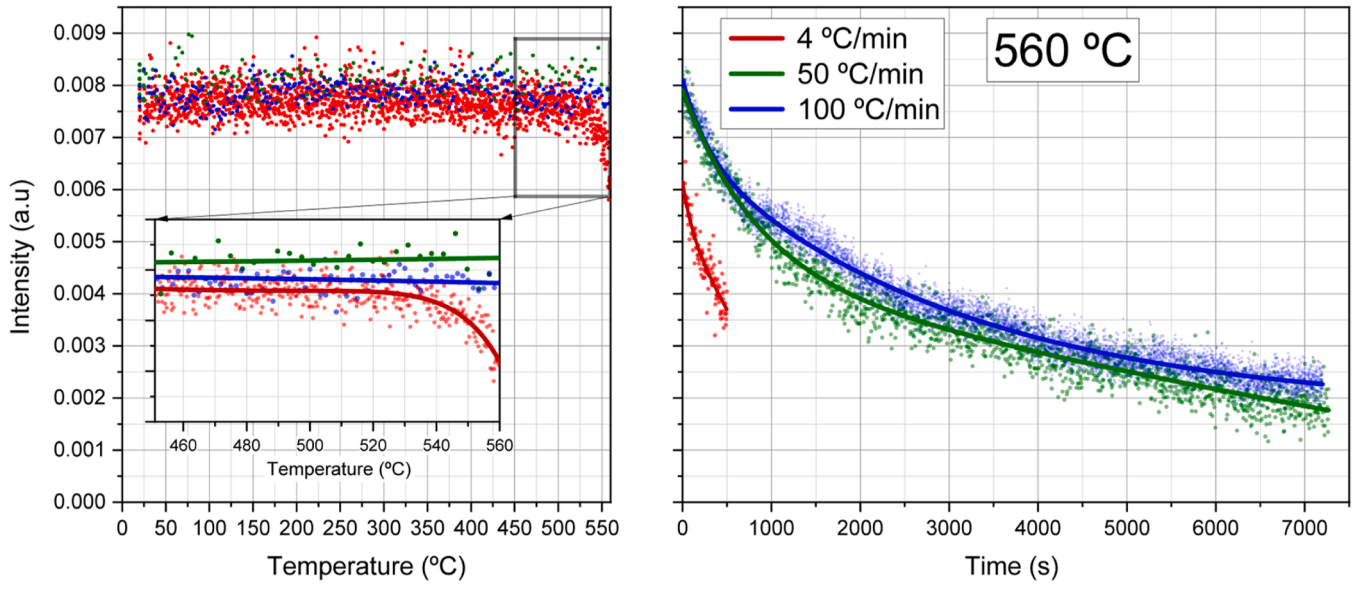

Fig. 7. Evolution of β as a function of temperature from room temperature to 560 °C at three heating rates (4, 50, and 100 °C/min), including an isothermal holding stage at 560 °C.

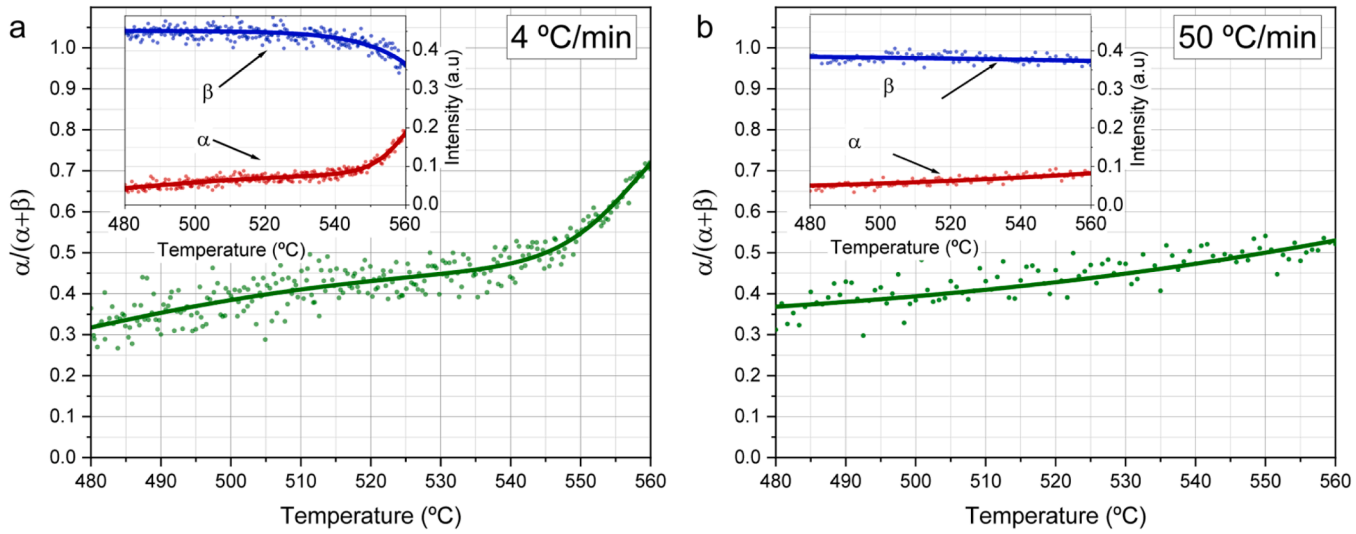

Fig. 8. Relative α fraction during the heating at 4 °C/min (a) and 50 °C/min (b) to 560 °C. The individual evolutions of α (red) and β (blue) are shown in the upper left corner of the figures.

occurs between 550 and 560 °C. Fig. 8b shows the relative fraction of α during the heating at 50 °C/min. At this faster rate, the relative α fraction increases from 0.37 at 480 °C to 0.53 at 560 °C, not exhibiting the rapid increase previously seen at 4 °C/min, as the fraction of β practically does not change.

The prolongation of the heating ramp at 50 °C/min until 600 °C is shown in Fig. 9. At 550 °C, the relative fraction of α is 0.5. It gradually increases to 0.6 at 585 °C, after which a rapid growth in α, coinciding with the start of β dissolution, raises its fraction to 0.8 by 600 °C. For both heating rates, 4 and 50 °C/min, the rapid increase in the α fraction coincides with the onset of β dissolution, which occurs at higher temperatures under the faster heating rate. The homogenization temperatures marking the start of the holding stage, as discussed in 3.3, are shown in Fig. 9 with dashed lines.

The differences between the evolution of α and β diffraction peaks during the heating stage indicate that at the onset of the β→α transformation, the nucleation and initial growth of α occur independently from β dissolution, the latter starting at 540 °C for the 4 °C/min and at 585 °C for the faster 50 °C/min. Therefore, the reported spatial relation between α nucleation and β particles may be, at the beginning of the heating, solely explained by the favorable energetic contributions of heterogeneous nucleation, followed by a second segment in which the dissolution of β accelerates the nucleation and growth of α in the microstructure.

3.3. *Effect of the homogenization temperature*

Fig. 10 presents the results of the α phase diffraction intensity evolution during the isothermal holding stage at the selected homogenization temperatures (540, 550, 560, 570, 580, 590, and 600 °C). The variation in α-phase intensity, determined from the diffraction signal of the (530) plane, is plotted for the selected heat treatments.

The evolution of α exhibits the characteristic parabolic time dependence associated with diffusion-controlled growth processes. The rate of α formation is accelerated at higher homogenization temperatures. Within the selected temperature range, α is the equilibrium intermetallic phase of the system, in agreement with the equilibrium calculation presented in Fig. 1b. At temperatures of 600 and 590 °C, the intensity of α reaches a maximum within 100 and 400 s, followed by a plateau,

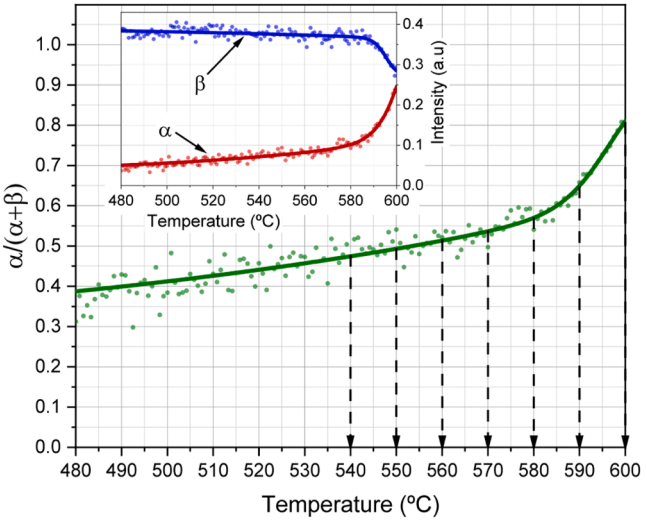

Fig. 9. Relative α fraction during the heating at 50 °C/min to 600 °C. The extent of the transformation at the chosen temperatures for the holding stage (540, 550, 560, 570, 580, 590, and 600 °C) is marked with dashed lines.

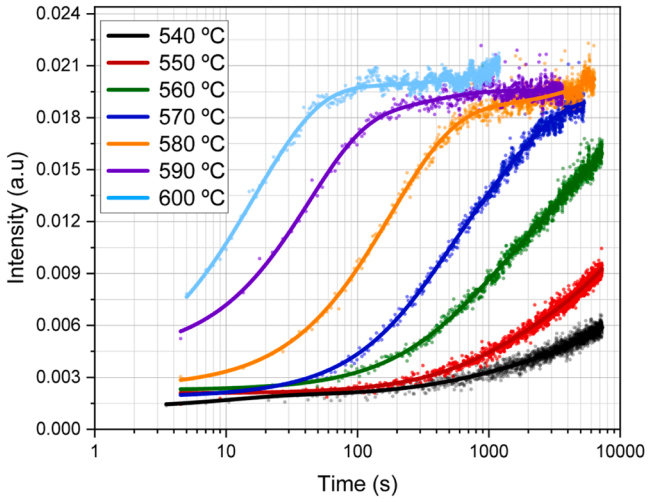

Fig. 10. Evolution of α over time at selected homogenization temperatures (540, 550, 560, 570, 580, 590, and 600 °C). The Initial diffraction intensity differs due to the previous heating ramp from room temperature at 50 °C/min.

suggesting that the phase has reached its thermodynamic equilibrium fraction in the system. The importance of industrial homogenization times on α phase evolution is evident at temperatures 540, 550, and 560 °C, where the intensity does not converge to the asymptotic region after 2 h, indicating that the thermodynamic equilibrium state has not yet been reached. The differences in the initial α intensity result from the heating stage to the homogenization temperature, as illustrated in Fig. 9.

The dissolution of (metastable) β with time at the selected isothermal temperatures is shown in Fig. 11. Analogous to α, β evolution takes place faster at higher homogenization temperatures. The transformation of β can also be explained by diffusion-related phenomena, following a parabolic time dependence. β-related peaks disappear from the diffractograms after 200 and 500 s at 600 and 590 °C, respectively, suggesting its complete dissolution. At the higher homogenization temperatures, the system reaches its equilibrium state shortly after the beginning of the isothermal stage, as the α phase also achieves its equilibrium fraction at this stage. For 580 and 570 °C, β dissolution occurs approximately after 1000 and 5000 s, respectively. The transformation at 540 °C is comparatively slower, reaching a 10 % signal reduction after 2 h, likely due to the more sluggish element diffusion. Following 2 h at 550 °C, a 40 % intensity drop is measured, while for homogenization at 560 °C, an 80 % β dissolution is achieved.

3.4. Quantification of the β→α transformation at the homogenization temperature

The calculated relative α fraction during the isothermal stage of the homogenization treatment is shown in Fig. 12. For all homogenization temperatures studied, during the holding stage, β tends to dissolve while the amount of α in the system increases. This indicates a positive driving force for the β→α transformation. As expected from the analysis of the intensity evolution, the transformation is completed in less than 500 s for 590 and 600 °C. By homogenizing at 570 and 580 °C, the relative α fraction reaches 1 after 1000 and 2500 s, respectively. After two h at 560 °C, α is almost entirely transformed. At 540 and 550 °C, a relative α fraction of 0.8 and 0.9 is reached, respectively.

The parabolic nature of the β and α evolution indicates a diffusional-based transformation. At higher temperatures, the rate at which the transformation proceeds, for a constant heating rate, increases. A calculation of β and α chemical driving forces in the Al matrix (Fig. 13a) reveals that the difference in driving force between β and α actually decreases, (though remaining a positive value) with increasing temperature.

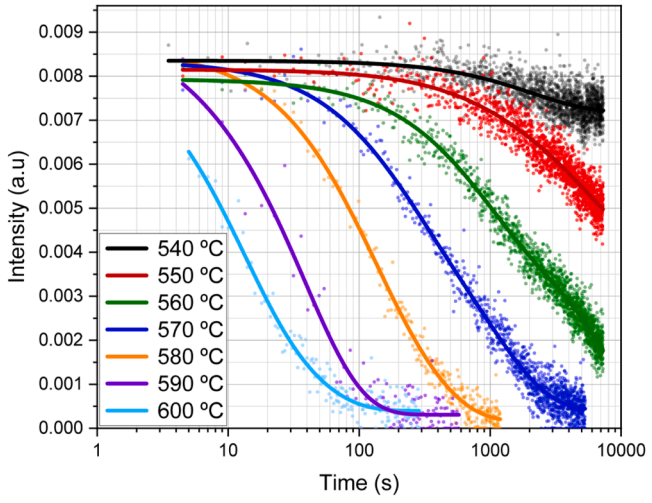

Fig. 11. Evolution of β over time at selected homogenization temperatures (540, 550, 560, 570, 580, 590, and 600 °C). The Initial diffraction intensity differs due to the previous heating ramp from room temperature at 50 °C/min.

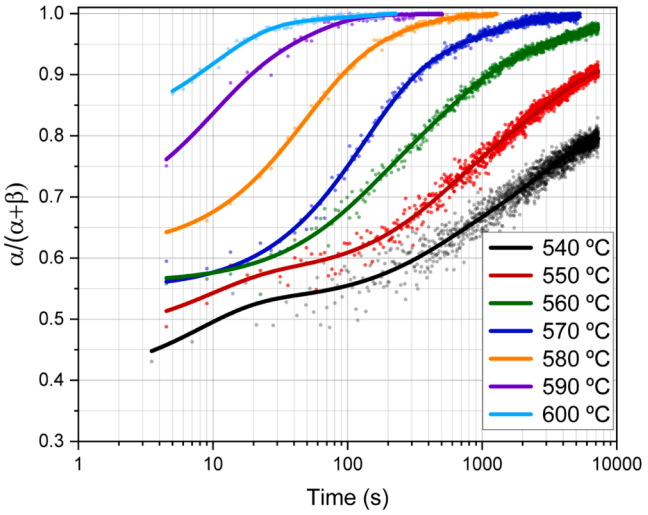

Fig. 12. Relative α fraction over time during the holding stage of the homogenization treatment at temperatures 540, 550, 560, 570, 580, 590, and 600 °C. The initial values reflect the extent of transformation achieved during the heating ramp to the holding temperature.

In contrast, at higher temperatures, the element diffusivity in the matrix increases. The element diffusion of Si, Fe, and Mn in the fcc matrix is calculated using the latest Al diffusion database in Matcalc [52], shown in Fig. 13b. The diffusion of Mn in the Al matrix at 550 °C is approximately 2 and 3 orders of magnitude lower than that of Fe and Si, respectively. Mn, being part of the α stoichiometry, may therefore be regarded as the limiting factor for α growth, and therefore for the β→α transformation. The kinetics of the transformation are controlled by the diffusion of Mn atoms from the bulk towards the α particle interface, being faster at higher temperatures.

4. Conclusions

The β→α transformation is studied using in-situ HEXRD under various heat treatment conditions. The effects of heating rate, holding temperature, and time are analyzed by measuring the intensity evolution from α and β-related diffraction peaks. The following is concluded:

- The onset of the β→α transformation occurs during the heating ramp to the homogenization temperature. At the slowest heating rate measured, 4 °C/min, two segments of α evolution are indicated. Initially, the α fraction increases from 430 °C onwards while the β fraction remains constant, suggesting that the first stage of α growth occurs independently from β dissolution. The second stage begins around 550 °C, when the rate at which α grows increases once β starts to dissolve. For the heating at 50 °C/min, this second segment is only observed starting from 585 °C.
- β is metastable in the system at all homogenization temperatures investigated (540–600 °C) and thus tends to dissolve, whereas the fraction of α, the stable intermetallic phase, increases towards its equilibrium in the system. At 590 and 600 °C, the β→α transformation is completed in less than 500 s. Below 570 °C, the maximum holding time studied of 2 h is insufficient to complete the transformation. The parabolic evolution of the reaction at isothermal holding indicates that the β→α transformation is diffusion-based. The kinetics of the process at the holding stage are most likely controlled by the diffusion of Mn atoms from the bulk to the α particle interface.

CRediT authorship contribution statement

Erwin Povoden-Karadeniz: Writing – review & editing, Supervision, Resources, Project administration, Investigation, Funding

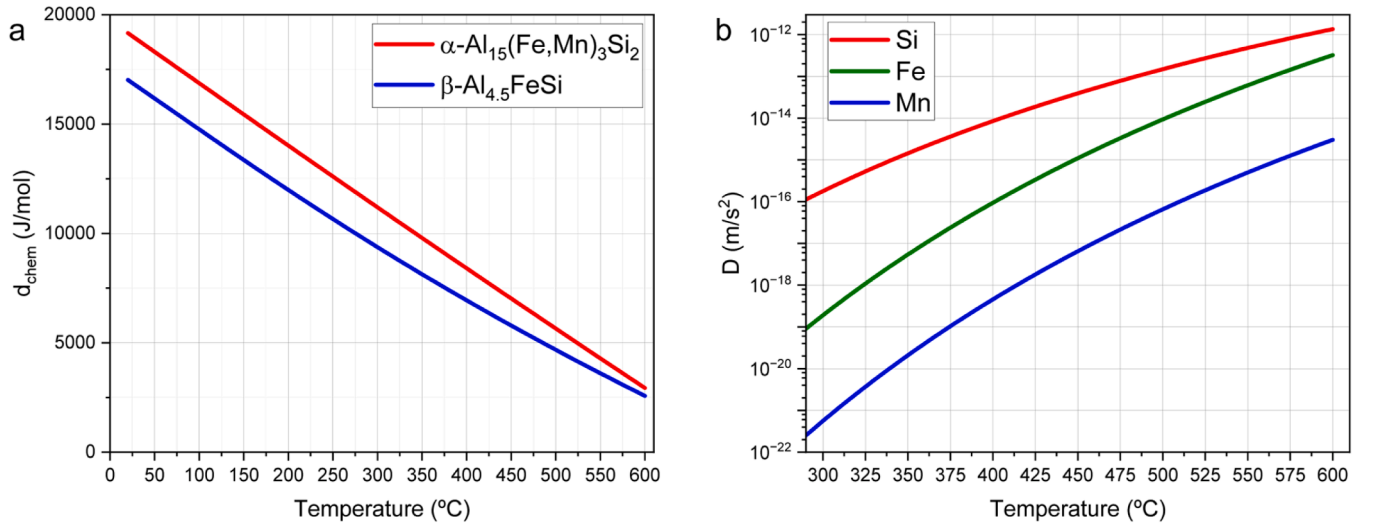

Fig. 13. a) Calculated chemical driving forces over temperature for the nucleation of β-$Al_{4.5}$FeSi and α-$Al_{15}(Fe,Mn)_3Si_2$ in the Al matrix. b) Calculated Si, Fe, and Mn diffusivity in the Al matrix as a function of temperature.

acquisition, Conceptualization. **Philipp Retzl:** Writing – review & editing, Methodology, Investigation, Conceptualization. **Andreas Stark:** Methodology, Investigation. **Lukas Helml:** Writing – review & editing, Methodology, Investigation, Conceptualization. **Nicolás García Arango:** Writing – review & editing, Writing – original draft, Visualization, Validation, Software, Methodology, Investigation, Formal analysis, Data curation, Conceptualization. **Roman Schuster:** Writing – review & editing, Methodology, Investigation, Conceptualization. **Robert Kahlenberg:** Writing – review & editing, Methodology, Investigation, Conceptualization. **Philipp Timm:** Writing – review & editing, Methodology, Investigation, Conceptualization.

Funding

The research was funded by Christian Doppler Forschungsgesellschaft in the framework of the CD-Laboratory of Interfaces and Precipitation Engineering (CDL-IPE).

Declaration of Competing Interest

The authors declare that they have no known competing financial interests or personal relationships that could have appeared to influence the work reported in this paper.

Acknowledgments

The financial support from the Austrian Federal Ministry for Digital and Economic Affairs and the National Foundation for Research, Technology, and Development is gratefully acknowledged. The authors acknowledge TU Wien Bibliothek for financial support through its Open Access Funding Programme. The authors gratefully acknowledge the financial support and the provision of sample material by Neuman Aluminium.

We acknowledge DESY (Hamburg, Germany), a member of the Helmholtz Association HGF, for the provision of experimental facilities. Parts of this research were carried out at the P07B High Energy Materials Science beamline at PETRA III. Beamtime was allocated for proposal I-20240466 EC.

References

[1] L. Lu, A.K. Dahle, Iron-rich intermetallic phases and their role in casting defect formation in hypoeutectic Al-Si alloys, J. Alloy. Compd. 36 (2005) 819–835, https://doi.org/10.1007/s11661-005-1012-4.
[2] G. Mrówka-Nowotnik, J. Sieniawski, M. Wierzbinska, Intermetallic phase particles in 6082 aluminium alloy, J. Alloy. Compd. 28 (2007) 69–76.
[3] L.F. Mondolfo. Aluminum alloys: structure and properties, Butterworths, 1976.
[4] H.W.L. Phillips, P.C. Varley, The constitution of alloys of aluminium with magnesium, silicon, and iron, J. Alloy. Compd. 72 (1946) 151–227.
[5] H. Tanihata, T. Sugawara, K. Matsuda, S. Ikeno, Effect of casting and homogenizing treatment conditions on the formation of Al-Fe-Si intermetallic compounds in 6063 Al-Mg-Si alloys, J. Mater. Sci. 34 (1999) 1205–1210, https://doi.org/10.1023/A:1004504805781.
[6] H. Becker, T. Bergh, P.E. Vullum, A. Leineweber, Y. Li, Effect of Mn and cooling rates on α-, β- and δ-Al–Fe–Si intermetallic phase formation in a secondary Al–Si alloy, Materialia 5 (2019), https://doi.org/10.1016/j.mtla.2018.100198.
[7] W. Khalifa, F. Samuel, J. Gruzleski, P. D. Student, Iron intermetallic phases in the Al corner of the Al-Si-Fe system, Metall. Mater. Trans. A 34 (2003) 807–825, https://doi.org/10.1007/s11661-003-0116-y.
[8] G. Sha, K. O'Reilly, B. Cantor, R. Hamerton, J. Worth, Effect of grain refiner on intermetallic phase formation in directional solidification of 6xxx series wrought Al alloys, Mater. Sci. Forum 331 (2000), https://doi.org/10.4028/www.scientific.net/msf.331-337.253.
[9] T. Smith, K. O'Reilly, S. Kumar, I. Stone, Influence of grain-refiner addition on the morphology of Fe-bearing intermetallics in a semi-solid processed Al-Mg-Si alloy, Metall. Mater. Trans. A 44 (2013) 4866–4871, https://doi.org/10.1007/s11661-013-1934-1.
[10] M.V. Kral, A crystallographic identification of intermetallic phases in Al-Si alloys, Mater. Lett. 59 (2005) 2271–2276, https://doi.org/10.1016/j.matlet.2004.05.091.
[11] S. Kumar, P.S. Grant, K.A.Q. O'Reilly, Fe bearing intermetallic phase formation in a wrought Al-Mg-Si alloy, Trans. Indian Inst. Met. (2012) 553–557, https://doi.org/10.1007/s12666-012-0221-y.
[12] M. Warmuzek, Primary crystals of AlFeMnSi intermetallics in the cast AlSi alloys, Arch. Metall. Mater. 62 (2017) 1659–1664, https://doi.org/10.1515/amm-2017-0254.
[13] Z. Ma, A.M. Samuel, H.W. Doty, S. Valtierra, F.H. Samuel, Effect of Fe content on the fracture behaviour of Al-Si-Cu cast alloys, Mater. Des. 57 (2014) 366–373, https://doi.org/10.1016/j.matdes.2014.01.037.
[14] X. Cao, J. Campbell, Morphology of β-Al5FeSi phase in Al-Si cast alloys, Mater. Trans. 47 (2006) 1303–1312, https://doi.org/10.2320/matertrans.47.1303.
[15] S. Zajac, B. Hutchinson, A. Johansson, L. Gullman, Microstructure control and extrudability of AI-Mg-Si alloys microalloyed with manganese, Mater. Sci. Technol. 10 (1994) 323–333, https://doi.org/10.1051/jp4:1993740.
[16] T. Gao, Y. Wu, C. Li, X. Liu, Morphologies and growth mechanisms of α-Al(FeMn)Si in Al-Si-Fe-Mn alloy, Mater. Lett. 110 (2013) 191–194, https://doi.org/10.1016/j.matlet.2013.08.039.
[17] J.E. Tibballs, J.A. Horst, C.J. Simensen, Precipitation of α-Al(Fe,Mn)Si from the melt, J. Mater. Sci. 36 (2001) 937–941, https://doi.org/10.1023/A:1004815621313.
[18] N. Belov, D. Eskin, A. Aksenov, Alloys of the Al-Fe-Mn-Si system. Multicomponent Phase Diagrams, 2005, p. 1.
[19] I. Todd, W. Kool, I.S. van der Zwaag, I.N.C.W. Kuijpers, Intermetallic phase transformations during homogenisation of 6xxx Al alloys: A literature review, Delft, 2000.
[20] N. García Arango, R. Schuster, R. Abart, E. Povoden-Karadeniz, Microanalysis-based simulation of heterogeneous dispersoid distribution in an Al alloy after the homogenization stage, Crystals 15 (2025) 695, https://doi.org/10.3390/cryst15080695.
[21] I. Polmear, D. John St., J.F. Nie, M. Qian, Light Alloys: Metallurgy of the Light. Metals, fifth ed., Butterworth-Heinemann, 2017.

[22] S. Onurlu, A. Tekin, Effect of heat treatment on the insoluble intermetallic phases present in an AA 6063 alloy, J. Mater. Sci. 29 (1994) 1652–1655, https://doi.org/10.1007/BF00368940.
[23] T. Radetić, M. Popović, A. Alil, B. Markoli, I. Naglič, E. Romhanji, Effect of homogenization temperature on microstructure and mechanical properties of Al-Mg-Si alloy containing low-melting point elements, J. Alloy. Compd. 902 (2022), https://doi.org/10.1016/j.jallcom.2022.163719.
[24] N.C.W. Kuijpers, W.H. Kool, P.T.G. Koenis, K.E. Nilsen, I. Todd, S. Van der Zwaag, Assessment of different techniques for quantification of α-Al(FeMn)Si and β-AlFeSi intermetallics in AA 6xxx alloys, Mater. Charact. 49 (2002) 409–420, https://doi.org/10.1016/S1044-5803(03)00036-6.
[25] I.G. Aguilar, J.T. Torres, A.F. Valdés, A.A.F. Saldivar, The effect of interrupted homogenization on β-Al5FeSi → α-Alx(Fe and Mn)Si transformation in the A6063 aluminum alloy, Met. (Basel) 12 (2022), https://doi.org/10.3390/met12122117.
[26] N.C.W. Kuijpers, J. Tirel, D.N. Hanlon, S. Van Der Zwaag, Quantification of the evolution of the 3D intermetallic structure in a 6005A aluminium alloy during a homogenisation treatment, Mater. Charact. 48 (2002) 379–392, https://doi.org/10.1016/S1044-5803(02)00289-9.
[27] P. Orozco-Gonzàlez, et al., Effect of iron addition on the crystal structure of the α-AlFeMnSi phase formed in the quaternary Al-Fe-Mn-Si system, Rev. Metal. (Madr.) 47 (2011) 453–461, https://doi.org/10.3989/revmetalm.1068.
[28] N. Bayat, T. Carlberg, M. Cieslar, In-situ study of phase transformations during homogenization of 6060 and 6063 Al alloys, J. Phys. Chem. Solids 130 (2019) 165–171, https://doi.org/10.1016/j.jpcs.2018.11.013.
[29] N.C.W. Kuijpers, F.J. Vermolen, C. Vuik, P.T.G. Koenis, K.E. Nilsen, S. van der Zwaag, The dependence of the β-AlFeSi to α-Al(FeMn)Si transformation kinetics in Al-Mg-Si alloys on the alloying elements, Mater. Sci. Eng. A 394 (2005) 9–19, https://doi.org/10.1016/j.msea.2004.09.073.
[30] P. Sedigh Rahimabadi, M. Khodaei, K.R. Koswattage, Review on applications of synchrotron-based X-ray techniques in materials characterization, John Wiley Sons Ltd (2020), https://doi.org/10.1002/xrs.3141.
[31] R. Schuster, et al., In-situ XRD investigation of σ phase precipitation kinetics during isothermal holding in a hyper duplex stainless steel, Mater. Charact. 203 (2023), https://doi.org/10.1016/j.matchar.2023.113124.
[32] S. Lin, U. Borggren, A. Stark, A. Borgenstam, W. Mu, P. Hedström, In-situ high-energy X-ray diffraction study of austenite decomposition during rapid cooling and isothermal holding in two HSLA steels, Metall. Mater. Trans. A 52 (2021) 1812–1825, https://doi.org/10.1007/s11661-021-06192-x.
[33] R. Kahlenberg, et al., Revisiting high-energy X-ray diffraction and differential scanning calorimetry data of EN AW-6082 with mean field simulations, Thermochim. Acta 740 (2024), https://doi.org/10.1016/j.tca.2024.179848.
[34] C. Rowolt, et al., In-situ analysis of continuous cooling precipitation in Al alloys by wide-angle X-ray scattering, Sci. Technol. Adv. Mater. 21 (2020) 205–218, https://doi.org/10.1080/14686996.2020.1739554.
[35] H. Fröck, et al., In situ high-energy X-ray diffraction of precipitation and dissolution reactions during heating of Al alloys, J. Mater. Sci. 56 (2021) 19697–19708, https://doi.org/10.1007/s10853-021-06548-z.
[36] N. García Arango, et al., In-situ HEXRD analysis of Al alloy EN AW-6082 during homogenization, J. Mater. Res. Technol. 38 (2025) 5026–5035, https://doi.org/10.1016/j.jmrt.2025.08.298.
[37] M. Dehmas, P. Weisbecker, G. Geandier, P. Archambault, E. Aeby-Gautier, Experimental study of phase transformations in 3003 aluminium alloys during heating by in situ high energy X-ray synchrotron radiation, J. Alloy. Compd. 400 (2005) 116–124, https://doi.org/10.1016/j.jallcom.2005.03.062.
[38] E. Kozeschnik, MatCalc: solid state and precipitation kinetics simulation software, available at ⟨http://www.matcalc.tuwien.at⟩ (accessed November 1, 2025).
[39] Open-license multi-component MatCalc thermodynamic database mc_al version 2.035, Institute of Materials Science and Technology, TU Wien, Vienna, 2023. Available at ⟨https://www.matcalc.at/images/stories/Download/Database/mc_al_v2.035.tdb⟩ (accessed November 1, 2025).
[40] N. Schell, A. King, F. Beckmann, T. Fischer, M. Müller, A. Schreyer, The high energy materials science beamline (HEMS) at PETRA III, Mater. Sci. Forum Trans. Tech. Publ. 772 (2014) 57–61, https://doi.org/10.4028/www.scientific.net/MSF.772.57.
[41] A.P. Hammersley, FIT2D: A multi-purpose data reduction, analysis and visualization program, J. Appl. Crystallogr 49 (2016) 646–652, https://doi.org/10.1107/S1600576716000455.
[42] T. Degen, M. Sadki, E. Bron, U. König, G. Nénert, The high score suite, Powder Diffr. 29 (2014) S13–S18, https://doi.org/10.1017/S0885715614000840.
[43] K. Sugiyama, N. Kaji, K. Hiraga, Re-refinement of α-(AlMnSi), Acta Crystallogr. Sect. C. Cryst. Struct. Commun. 54 (1998) 445–447, https://doi.org/10.1107/S0108270197015989.
[44] M. Cooper, K. Robinson, The crystal structure of the ternary alloy α (AlMnSi), Acta Cryst. 20 (1966) 614–617, https://doi.org/10.1107/S0365110X6600149X.
[45] C. Romming, V. Hansen, J. Gjonnes, Crystal structure of β-Al4.5FeSi, Acta Cryst. B 50 (1994) 307–312, https://doi.org/10.1107/S0108768193013096.
[46] V. Hansen, B. Hauback, M. Sundberg, C. Romming, J. Gjonnes, β-Al4.5FeSi: a combined synchrotron powder diffraction, electron diffraction, high-resolution electron microscopy and single-crystal X-ray diffraction study of a faulted structure, Acta Cryst. B (1998).
[47] S.N. Kabekkodu, A. Dosen, T.N. Blanton, PDF-5+: a comprehensive Powder Diffraction FileTM for materials characterization, Powder Diffr. 39 (2024) 47–59.
[48] B.D. Cullity, S.R. Stock, Elements of X-ray Diffraction, third ed., Pearson, 2014.
[49] J.M. Cowley, Diffuse scattering and absorption effects. Diffraction Physics, third ed., 1995, pp. 257–285. North-Holland.
[50] R.L. Snyder, The use of reference intensity ratios in X-ray quantitative analysis, Powder Diffr. 7 (1992) 186–193, https://doi.org/10.1017/S0885715600018686.
[51] N. Bayat, T. Carlberg, M. Cieslar, In-situ study of phase transformations during homogenization of 6005 and 6082 Al alloys, J. Alloy. Compd. 725 (2017) 504–509, https://doi.org/10.1016/j.jallcom.2017.07.149.
[52] Open-license multi-component MatCalc diffusion mobilities database mc_al version 2.005, Institute of Materials Science and Technology, TU Wien, Vienna, 2023. Available at: ⟨https://www.matcalc.at/images/stories/Download/Database/mc_al_v2.005.ddb⟩ (accessed November 1, 2025).